第 54 卷第 4 期
2026 年 4 月

硅 酸 盐 学 报
JOURNAL OF THE CHINESE CERAMIC SOCIETY

Vol. 54，No. 4
April，2026

http://jccsoc.cbpt.cnki.net

DOI：10.14062/j.issn.0454-5648.20250810

$Pb(Zr_xTi_{1-x})O_3$ 铁电基自驱动紫外光电探测器的制备与性能

王梓赫，黄敏捷，张清风

(湖北大学材料科学与工程学院，武汉 430062)

摘 要：传统自供电紫外光探测器通常基于 p–n 结或肖特基结界面效应设计，然而由于光生电子和空穴无法有效分离，其响应度和探测率往往较低。与半导体材料不同，铁电材料通常拥有起源于自身大剩余极化强度且能贯穿整体的高退极化电场，因此可实现光生电子与空穴有效分离。基于此，本工作通过溶胶–凝胶工艺精准调控锆钛比例，制备出了不同锆钛比的 $Pb(Zr_xTi_{1-x})O_3$(PZT)铁电薄膜和光电性能优异的 Au/PZT/FTO 自驱动紫外光电探测器，并系统研究了组分对薄膜晶体结构、表面形貌、铁电性能及器件光电响应特性的影响规律。微结构测试表明：不同锆钛比的 PZT 薄膜均拥有优良的结晶质量和纯的钙钛矿相结构，且薄膜表面平整致密。铁电性能测试揭示：所有组分的 PZT 薄膜均展现出了良好的铁电性(退极化电场)且最大剩余极化强度高达 32.1 μC/cm^2。光电测试结果发现：当锆钛比为 0.52 : 0.48 时，器件的光电性能最为优异，在 320 nm 紫外光间歇照射下表现出稳定且可重复的光电流响应，且在–2 V 电压极化下，器件的响应度和探测率均显著提升。

关键词：锆钛酸铅；铁电薄膜；溶胶–凝胶；自驱动紫外光电探测器
中图分类号：O484.4　　**文献标志码**：A　　**文章编号**：0454–5648(2026)04–1202–08
网络出版时间：2026–03–09

随着时代的发展，紫外光电探测器在环境监测、通信安全等领域的应用需求不断增长，其性能要求也随之日益提高。在此背景下，为满足能源节约与器件小型化的需求，自驱动紫外光电探测器应运而生。然而，大多数传统的自驱动紫外光电探测器仍面临光生载流子分离效率低、光电响应性能差及响应速度受限等问题。具有较大剩余极化强度的铁电薄膜，能在体内形成贯穿整个块体的退极化电场，因此内部产生的光生电子与空穴可以效分离，从而为解决上述问题提供了有效途径[1–2]。此外，铁电薄膜基光电探测器还具有光电流可通过极化调控等优点，因此近年来备受研究者关注[2–3]。$Pb(Zr_xTi_{1-x})O_3$ (PZT) 是一类典型的 ABO_3 型钙钛矿铁电材料，以其优异的铁电、压电及光电性能，被广泛应用于铁电存储器、微机电系统和光电探测器等领域[2–5]。PZT 晶体结构由位于 A 位的 Pb^{2+}、B 位的 Zr^{4+}/Ti^{4+} 及面心的 O^{2-}共同构成。当 B 位离子偏离氧八面体中心时，晶胞内部会产生电偶极矩，形成自发极化。该极化方向可在外部电场作用下发生翻转，并呈现出典型的电滞回线特征[2]。这种独特的可逆极化行为，使得 PZT 薄膜能够通过其内建极化场有效分离光生载流子，从而展现出优异的光电响应潜力。

目前，国内外已有大量研究致力于探索成分对 PZT 薄膜性能的影响。例如，钟世兴等[6]发现成分对 PZT 薄膜的介电和铁电性能有着显著影响。Kweon 等[7]采用溅射工艺系统研究了 PZT 薄膜的成分调控规律，发现适当调整锆钛摩尔比能够显著改变薄膜的铁电与压电响应。综上所述，成分对 PZT 薄膜的晶相结构及铁电性能均具有重要影响，但对光电性能的影响需进一步系统研究。本工作拟针对不同锆钛比的 PZT 薄膜的光电特性进行分析，以揭示组分调控对光电效应的影响规律。

1 实验

1.1 原材料

所使用的实验试剂以及生产厂商如表 1 所示。

收稿日期：2025–11–07。　修订日期：2025–12–15。
基金项目：国家自然基金(52572127，52172113)；湖北省科技创新基地(平台)项目(2025CSA140)。
第一作者：王梓赫(2002—)，男，硕士研究生。
通信作者：张清风(1983—)，男，教授。

Received date: 2025–11–07.　**Revised date:** 2025–12–15.
First author: WANG Zihe (2002–), male, Master candidate.
E-mail: 627527318@qq.com
Correspondent author: ZHANG Qingfeng (1983–), male, Professor.
E-mail: zhangqingfeng@126.com

表 1　所用原材料信息

Table 1　Raw materials information

Material	Molecular weight	Purity/%	Manufacturer
$Pb(CH_3COO)_2{\cdot}3H_2O$	379.33	99.5	Sinopec Group
$C_{12}H_{28}O_4Ti$	284.22	95.0	Macklin
$C_{12}H_{28}O_4Zr$	327.57	70.0	Aladdin
$CH_3CH_2CH_2OH$	60.10	99.0	Aladdin
CH_3COOH	60.05	99.9	Sinopec Group

1.2　实验部分

1.2.1　PZT 薄膜基光电探测器的制备　　采用溶胶–凝胶法制备不同锆钛比的 PZT 铁电薄膜。所选前驱体与溶剂包括：高纯度醋酸铅[$Pb(CH_3COO)_2{\cdot}3H_2O$]、正丙醇锆($C_{12}H_{28}O_4Zr$)和钛酸异丙酯($C_{12}H_{28}O_4Ti$)分别作为铅、锆、钛源，冰醋酸($CH_3COOH$)作为螯合剂，正丙醇($CH_3CH_2CH_2OH$)作为稳定剂。具体流程为：首先，为补偿退火过程中的铅损失，在称量时额外加入了 20%(摩尔分数)的醋酸铅。将醋酸铅溶于冰醋酸后，在恒温磁力搅拌台上搅拌 30 min 至完全溶解。待溶液冷却至 25 ℃后，依次加入计量好的钛酸异丙酯和正丙醇锆，并添加 5 mL 去离子水以促进水解缩合。随后，在常温持续机械搅拌 30 min，再补加 15 mL 正丙醇以调节溶液极性。所得溶液经 2 h 搅拌后，静置陈化 24 h，完成从溶胶到凝胶的转变。将制备好的凝胶旋涂于 FTO 衬底上，匀胶程序设置为低速 500 r/min、6 s，随后高速 3000 r/min、30 s。随后，将湿膜依次在 150 ℃和 400 ℃的加热台上分别预退火 5 min 和 10 min。上述旋涂与预退火步骤重复 3 次，以获得所需厚度。最后，将薄膜在马弗炉中于 650 ℃退火 30 min，从而获得结晶质量良好的 PZT 薄膜。器件制备采用北京微纳真空技术有限公司的高真空热蒸镀仪(VZZ-300)，通过边长为 0.05 cm 的正方形掩膜板在薄膜表面沉积半透明金电极，最终制得 Au/PZT/FTO 垂直结构的自供电紫外光电探测器。

1.2.2　表征与测试　　采用 X 射线衍射仪(XRD，D8 Advance，Bruker，美国)对薄膜的晶体结构进行表征。薄膜的表面粗糙度通过原子力显微镜(AFM，Bruker Dimension Edge，美国)获得。利用紫外–可见–近红外分光光度计(UV–Vis–NIR，UV-3600 Plus，Shimadzu，日本)获取薄膜光学特性。铁电特性的获得是利用铁电测试系统(Precision LC Ⅱ，Radiant，美国)。通过 Keithley2400 数字源表获得电流–时间(I–t)曲线，并采用 150 W 紫外增强型氙灯作为光源。

2　结果与讨论

2.1　$Pb(Zr_xTi_{1-x})O_3$ 薄膜结构与表面形貌分析

图 1 为 $Pb(Zr_xTi_{1-x})O_3$ 薄膜 XRD 谱。由图 1 可见，所制备的 3 种不同锆钛比的 PZT 薄膜均呈现典型钙钛矿结构，并且除 FTO 基底的衍射峰外，未检测到任何杂相的峰。2θ≈21.9°、31.0°、45.1°和 55.8°处的衍射峰分别对应于 PZT 的(001)、(110)、(002)和(211)晶面。这些衍射峰形尖锐且强度高，表明所制备的 PZT 薄膜具有优异的结晶质量。这主要归因于前驱体溶液中额外引入了 20%(摩尔分数)的 Pb^{2+}，有效的补偿了退火过程中 Pb^{2+}的挥发损失。

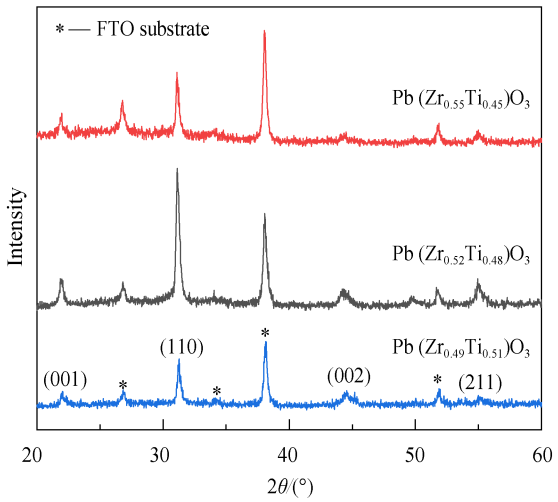

图 1　$Pb(Zr_xTi_{1-x})O_3$ 薄膜的 XRD 谱

Fig. 1　XRD patterns of $Pb(Zr_xTi_{1-x})O_3$ thin films

图 2 为 $Pb(Zr_xTi_{1-x})O_3$ 薄膜的三维表面形貌。如图 2 所示，随着 Zr 含量的增加，薄膜表面形貌经历了显著演化：从细长的针尖状结构，逐渐转变为岛状结构，最终形成波浪状起伏。这一形貌演化主要归因与 Zr^{4+}(0.72 Å)和 Ti^{4+}(0.605 Å)的离子半径差异。半径较大的 Zr^{4+}会引起晶格膨胀与畸变，进而改变了晶体表面微观结构的形成难度，从而驱动了形貌的变化。尽管形貌随组分变化，所有薄膜均表现出良好的表面质量，未观察到明显的缺陷、孔洞、污染或团聚现象，表明其具有优异的平整度与连续性。粗糙度分析进一步证实了这一点：所有薄膜的均方根(RMS)粗糙度均低于 3 nm，且随锆钛比增加呈先降后升的趋势。当锆钛比为 0.52∶0.48 时，获得了最低的 RMS 粗糙度，仅为 2.62 nm。

2.2　$Pb(Zr_xTi_{1-x})O_3$ 薄膜的铁电性能分析

图 3 为 $Pb(Zr_xTi_{1-x})O_3$ 薄膜在室温测得的电滞(P–E)回线。所有样品均呈现出了典型的铁电回线

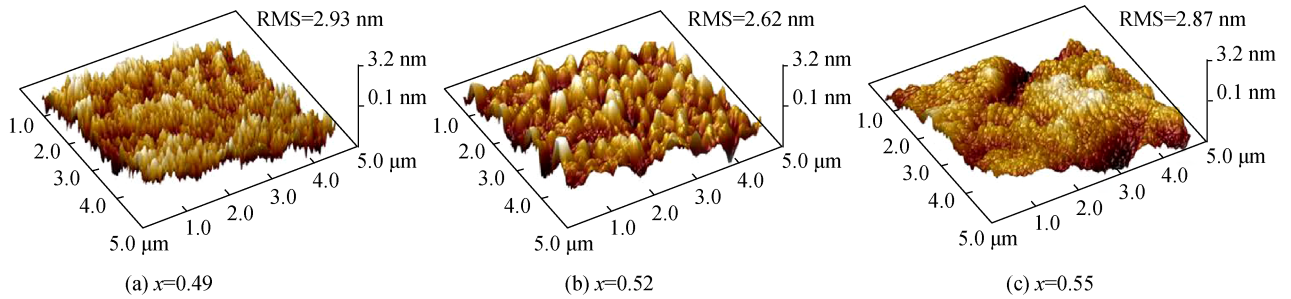

RMS is root mean square roughness.

图 2 $Pb(Zr_xTi_{1-x})O_3$ 薄膜的三维表面形貌

Fig. 2 3D surface morphology of $Pb(Zr_xTi_{1-x})O_3$ thin films

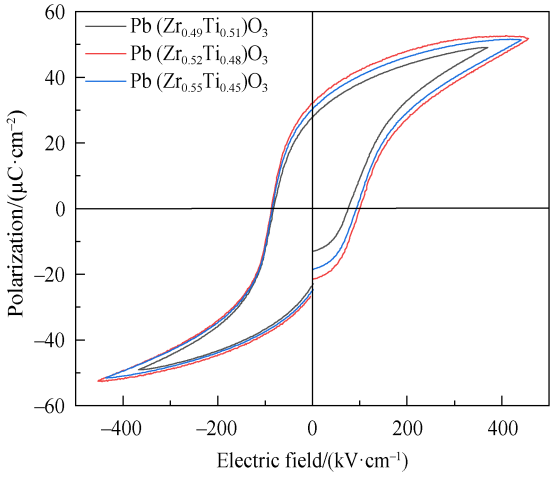

图 3 $Pb(Zr_xTi_{1-x})O_3$ 薄膜的室温电滞回线

Fig. 3 Room-temperature *P*–*E* curves of $Pb(Zr_xTi_{1-x})O_3$ thin films

特征，且剩余极化值均超过 27 μC/cm²。这说明所制备的 PZT 薄膜具有良好的铁电性能，并因此有助于增强光电探测器中的光生载流子分离。随着 Zr 含量的增加，剩余极化值先升高后下降：从 27.9 μC/cm² (Zr/Ti=0.49/0.51)上升至最大值 32.1 μC/cm² (Zr/Ti=0.52/0.48)，随后下降至 30.2 μC/cm² (Zr/Ti=0.55/0.45)。该现象可归因于 B 位离子尺寸效应与晶胞体积变化的竞争机制。在 PZT 钙钛矿结构中，极化源于 B 位离子的偏心位移。虽然半径较大的 Zr^{4+} (0.72 Å)的引入会导致 B 位离子的偏心位移，但其引起的晶胞体积膨胀效应占主导时，会促使电偶极子在外电场下更易翻转，从而提高极化强度。然而，当锆钛比增至 0.55∶0.45 时，B 位离子半径增大对偶极子翻转的阻碍效应超过了晶胞膨胀的积极作用，最终导致极化强度下降[2, 8–9]。较高的剩余极化值有利于形成更强的内建电场，能有效抑制光生载流子的复合，提高其分离效率。这使得自驱动紫外探测器在零偏压下仍能维持较高的光响应性能，并且其光电流可通过极化方向进行调控，这部分验证将在后续内容中展开。

2.3 $Pb(Zr_xTi_{1-x})O_3$ 薄膜的光学性能分析

透射光谱是分析材料光透过特性及相应器件光谱响应行为的重要手段。通过分析透射光谱，不仅可以确定薄膜的光学吸收边，还能进一步推算其光学带隙与光吸收能力。图 4a 为不同锆钛比 PZT 薄

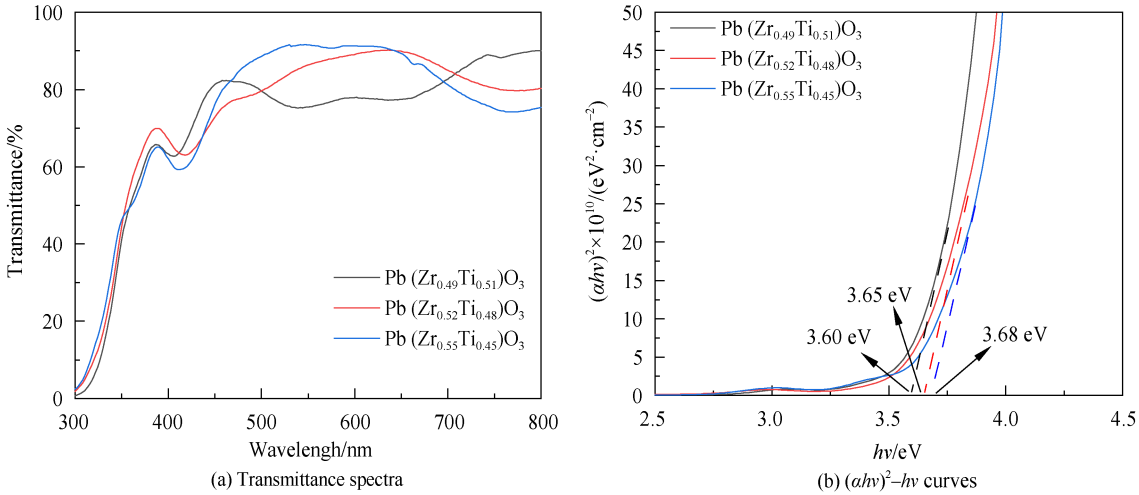

图 4 $Pb(Zr_xTi_{1-x})O_3$ 薄膜的光学特性

Fig. 4 Optical properties of $Pb(Zr_xTi_{1-x})O_3$ thin films

膜在 300~800 nm 波长范围内的透射光谱。所有组分的薄膜在可见光波段均表现出较高的透光率，而在紫外光波段内，透射率急剧下降，呈现出陡峭的吸收边，这表明 PZT 薄膜对紫外光有强吸收。随着 Zr 含量的增加，吸收边明显向短波长方向(蓝移)，这预示着 Zr 掺杂可有效调控 PZT 的带隙。基于透射光谱数据，借助 Tauc 关系式[10–12]，可计算出 PZT 薄膜的光学带隙，如式(1)所示：

$$(\alpha hv)^2 = A(hv - E_g) \tag{1}$$

式中：A 为常数；hv 为入射光子的能量；α 为吸收系数；E_g 为光学带隙。根据薄膜的透射光谱，可绘制$(\alpha hv)^2$ 与 hv 的关系曲线，如图 4b 所示。由图 4b 可见，不同锆钛比的 PZT 薄膜均为宽禁带半导体(>3.6 eV)，且随着 Zr 含量的增加，薄膜的带隙值从 3.60 eV 增大至 3.68 eV，呈现蓝移趋势。该变化规律可由组分效应合理解释：由于 $PbZrO_3$ 的带隙(4.0~4.5 eV)大于 $PbTiO_3$ 的带隙(3.4~3.6 eV)[13–14]，因此随着 Zr 含量的增加，PZT 薄膜的带隙随之增大，导致吸收边发生蓝移。

2.4　$Pb(Zr_xTi_{1-x})O_3$ 基自驱动紫外光电探测器性能

图 5 为不同极化电压下 $Pb(Zr_xTi_{1-x})O_3$ 薄膜的光电响应特性。测试在波长为 320 nm 的间歇性紫外光照射下进行。实验中，将在 PZT 薄膜上的 Au 电极施加正电压时的极化定义为正极化。鉴于不同锆钛比薄膜的极化与耐压特性不同，所施加的极化电压范围分别为±2 V、–2 V 与+3 V 以及±2 V。结果显示，所有器件在光照下均表现出快速的响应与恢复特性，并在多周期测试中展现了良好的稳定性与重复性。光电流强度显著受极化电压调控：当施加负极化电压时，PZT 内部退极化电场与界面肖特基势垒引起的内建电场方向一致，协同增强了载流子分离驱动力，从而使光电流显著增加；反之，施加正极化电压时，二者因方向相反而相互抵消，抑制了载流子分离，导致光电流减小[15–16]。特别值得注意的是，对于锆钛比为 0.52∶0.48 的样品，在施加–2 V 极化电压时，其显著增强，峰值达到 7.1 nA。这一优异性能归因于该组分薄膜具有最高的剩余极化强度(图 3)，从而能在光照下实现更高效的光生载流子分离与传输。

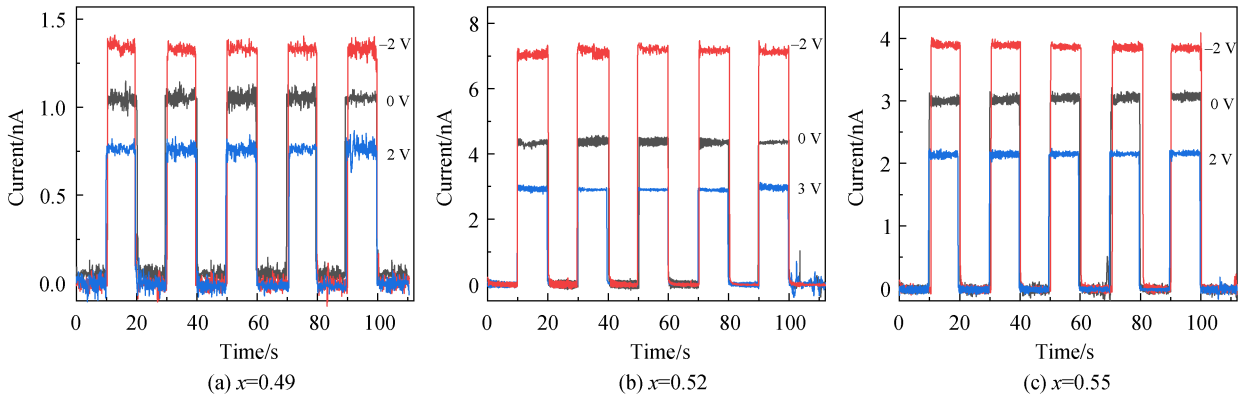

图 5　$Pb(Zr_xTi_{1-x})O_3$ 基光电探测器在不同极化电压下的 I–t 曲线

Fig. 5　I–t curves of $Pb(Zr_xTi_{1-x})O_3$ based photodetectors under various poling voltages

光电探测器的性能优劣不仅取决于光电流的大小，还需通过响应度(Responsivity, R)与探测率(Detectivity, D^*)2 个关键参数进行综合评估。响应度反映其光电转换效率，而探测率则表征器件在噪声背景下检测微弱光信号的能力，体现其灵敏度与抗干扰性能。本工作在 200~600 nm 波长范围内对器件进行了系统的光谱响应测试，并基于式(2)和式(3)计算出响应度与探测率[17–18]：

$$R = \frac{I_{light} - I_{dark}}{P_\lambda S} \tag{2}$$

$$D^* = \frac{R_\lambda \sqrt{S}}{\sqrt{2eI_{dark}}} \tag{3}$$

式中：I_{light} 为光电流；I_{dark} 为暗电流；P_λ 为入射光功率；S 为有效受光面积；e 为电子电荷。图 6 为 $Pb(Zr_xTi_{1-x})O_3$ 基光电探测器在不同极化电压下的响应度与探测率变化规律。当锆钛比为 0.52∶0.48 时，器件表现出最优性能，其在 320 nm 处的响应度和探测率分别达到 1.58 mA/W 和 0.23×10^{11} Jones。在施加负向极化电压后，该组分的性能提升最为显著，分别进一步提升至 3.4 mA/W (@300 nm)

和 0.36×10^{11} Jones。这主要归因于该组分器件能产生最大的光电流。

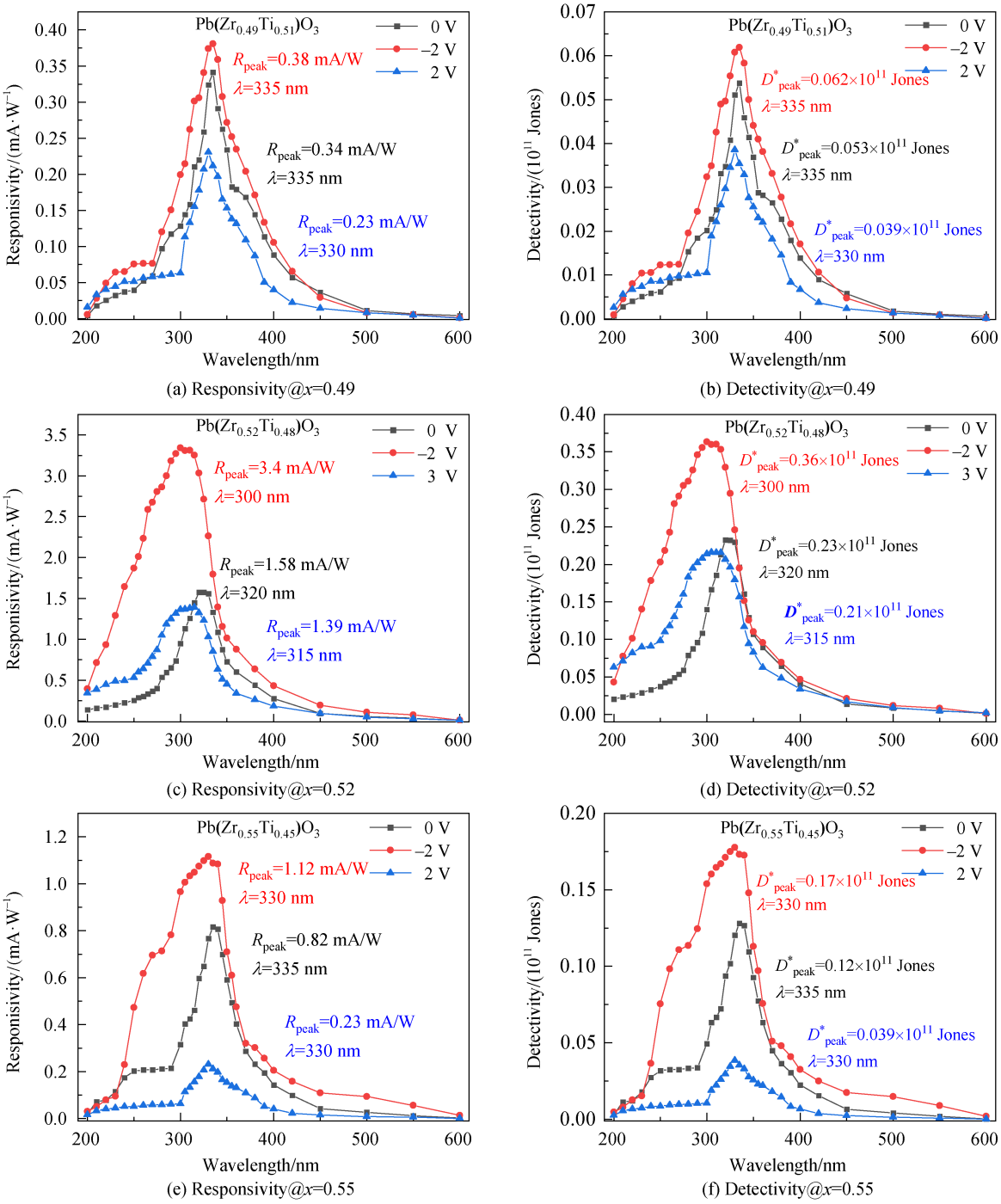

Note: R_{peak} and D^*_{peak} are the maximum values of responsivity and detectivity, respectively

图 6 $Pb(Zr_xTi_{1-x})O_3$ 基光电探测器在不同极化电压下的光电响应特性

Fig. 6 Photoresponse properties of $Pb(Zr_xTi_{1-x})O_3$ based photodetectors under different poling voltages

为评估所制备的铁电光电探测器的弱光探测能力，测试了经–2 V 电压极化的 $Pb(Zr_{0.52}Ti_{0.48})O_3$ 器件在 320 nm 波长、不同光功率密度下的时间响应特性(*I*–*t* 曲线)。如图 7a 所示，该器件在所有光强条件下均表现出优异的响应重复性与稳定性。特别地，即使在低至 0.17929 mW/cm^2 的弱光照射下，器件仍能产生 1.02 nA 的光电流，展现出卓越的探测灵敏度。另外，I_{light} 与 P_λ 呈现的幂律关系($I_{light} \propto P_\lambda^{0.78}$)，表明 Au/PZT/FTO 异质结具有高效的光生载流子分离与输运特性(图 7b)。器件响应度和探测率随着光功率密度减少而呈现出的明显提升，凸显了其在低光强检测场景中的优势。

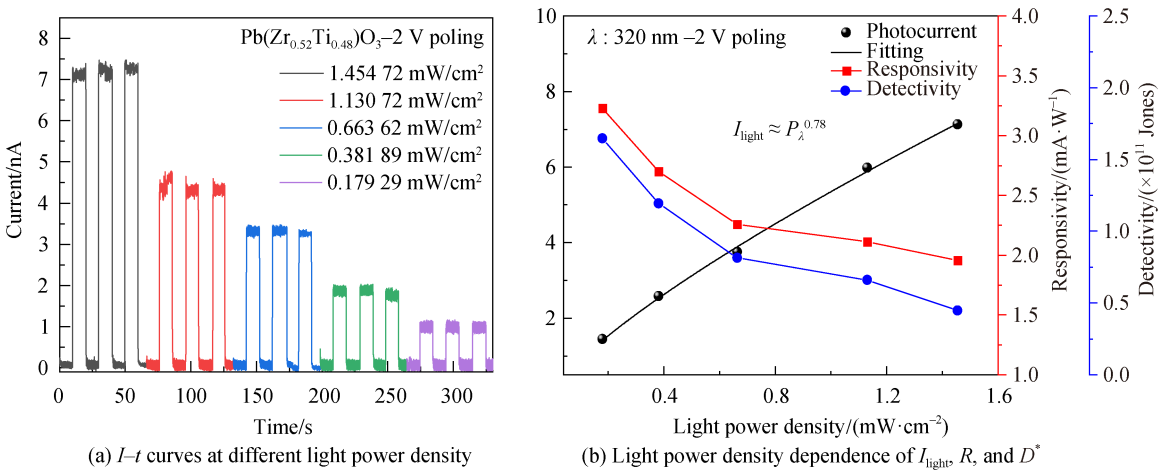

(a) *I*–*t* curves at different light power density　　(b) Light power density dependence of I_{light}, *R*, and D^*

图 7　$Pb(Zr_{0.52}Ti_{0.48})O_3$ 基光电探测器在极化电压为–2 V 和不同光照强度下光电响应特性

Fig. 7　Photoresponse properties the $Pb(Zr_{0.52}Ti_{0.48})O_3$ based photodetector under a poling voltage of –2 V and different light power density

3　结论

采用溶胶–凝胶法制备了不同锆钛比(Zr/Ti=0.49 : 0.51, 0.52 : 0.48, 0.55 : 0.45)的 $Pb(Zr_xTi_{1-x})O_3$ 铁电薄膜，并成功构建了 Au/PZT/FTO 结构的自驱动紫外光电探测器。结构表征表明，所有组分的 PZT 薄膜均呈现纯钙钛矿相，结晶质量良好。AFM 分析显示薄膜表面平整致密，颗粒分布均匀。铁电性能测试进一步证实，不同锆钛比的薄膜均表现出典型的电滞回线特征，并具有较高的剩余极化强度，其中在 Zr/Ti 为 0.52 : 0.48 时达到最大值 32.1 μC/cm²。光电测试结果表明，基于该组分的器件在 320 nm 紫外光间歇照射下，表现出稳定、可重复的光电流响应；尤其在–2 V 极化电压条件下，其光响应度与探测率均得到显著提升。综上，合理调控锆钛比可有效优化 PZT 薄膜的铁电性能与器件的光电特性。本工作创新性地利用 PZT 铁电体固有的体相退极化电场作为驱动力，实现了光生电子–空穴对的高效分离，更从组分设计、极化调控等角度提供了系统的优化方法，为突破自驱动紫外光电探测器低响应度、低探测率的关键瓶颈提供了一种有效的材料与物理机制解决方案。

参考文献:

[1] JIA W, REN H L, LI T B, et al. Fabrication of porous Ga_2O_3/GaN heterojunction for ultraviolet photodetector application[J]. Opt Express, 2025, 33(9): 18993–19003.

[2] ZHANG Y, CHEN J, CAI Y X, et al. Depolarization electric field and poling voltage-modulated Pb, La(Zr, Ti)O_3-based self-powered ultraviolet photodetectors[J]. J Am Ceram Soc, 2021, 104(2): 928–935.

[3] CHENG Y Y, MAO J X, DONG Y H, et al. Ferroelectric depolarization-field-enhanced Ag/ZnO/Si∶Ga_2O_3/BFMO/FTO multijunction self-driven photodetector with ultrahigh performance[J]. ACS Photonics, 2024, 11(11): 4786–4796.

[4] LIPATOV A, SHARMA P, GRUVERMAN A, et al. Optoelectrical molybdenum disulfide (MoS_2): Ferroelectric memories[J]. ACS Nano, 2015, 9(8): 8089–8098.

[5] YANG J L, MAO Y J, QU B B, et al. Dynamic responses of normal and partially failed piezoelectric stack actuators under sinusoidal voltages with DC biasing[J]. Smart Mater Struct, 2024, 33(9): 095004.

[6] 钟世兴, 蔡苇, 符春林, 等. 组成对锆钛酸铅铁电薄膜电性能影响的研究进展[J]. 硅酸盐通报, 2013, 32(7): 1306–1310.
ZHONG Shixing, CAI Wei, FU Chunlin, et al. Bull Chin Ceram Soc, 2013, 32(7): 1306–1310.

[7] KWEON S H, KIM E J, TAN G, et al. Compositional modification of epitaxial Pb(Zr, Ti)O_3 thin films for high-performance piezoelectric energy harvesters[J]. Adv Mater Interfaces, 2024, 11(31): 2400384.

[8] GONG W, LI J F, CHU X C, et al. Combined effect of preferential orientation and Zr/Ti atomic ratio on electrical properties of $Pb(Zr_xTi_{1-x})O_3$ thin films[J]. J Appl Phys, 2004, 96(1): 590–595.

[9] MORIOKA H, YOKOYAMA S, OIKAWA T, et al. Spontaneous polarization change with Zr/(Zr+Ti) ratios in perfectly polar-axis-orientated epitaxial tetragonal Pb(Zr, Ti)O_3 films[J]. Appl Phys Lett, 2004, 85(16): 3516–3518.

[10] ZHANG M, XU M J, LI M K, et al. SnO_2 epitaxial films with varying thickness on c-sapphire: Structure evolution and optical band gap modulation[J]. Appl Surf Sci, 2017, 423: 611–618.

[11] HE J, SUN L, CHEN S Y, et al. Composition dependence of structure and optical properties of $Cu_2ZnSn(S, Se)_4$ solid solutions: An experimental study[J]. J Alloys Compd, 2012, 511(1): 129–132.

[12] WANG Q L, HUANG P, LIU Q, et al. Ultra-wide-bandgap $(ScGa)_2O_3$ alloy thin films and related sensitive and fast responding solar-blind photodetectors[J]. J Alloys Compd, 2020, 834: 155036.

[13] LEE H, KANG Y S, CHO S J, et al. Dielectric functions and electronic band structure of lead zirconate titanate thin films[J]. J Appl Phys, 2005, 98(9): 094108.

[14] ZHENG T, DENG H M, ZHOU W L, et al. Optical bandgap reduction and ferromagnetic enhancement at room-temperature in $PbTi_{1-x}Fe_xO_{3-\delta}$ ferroelectrics[J]. Mater Lett, 2016, 185: 380–383.
[15] CHEN G, ZHANG Y, ZHANG Q F, et al. Superior ferroelectric photovoltaic properties in Fe-modified (Pb, La)(Zr, Ti)O_3 thin film by improving the remnant polarization and reducing the band gap[J]. Ceram Int, 2020, 46(10): 15061–15065.
[16] CHEN G, ZOU K L, YU Y X, et al. Effects of the film thickness and poling electric field on photovoltaic performances of (Pb, La)(Zr, Ti)O_3 ferroelectric thin film-based devices[J]. Ceram Int, 2020, 46(4): 4148–4153.
[17] PANDEY S, GANGULY S, SHUKLA A, et al. Enhanced UV photodetector efficiency with a ZnO/Ga_2O_3 heterojunction[J]. ACS Appl Electron Mater, 2025, 7(3): 1173–1181.
[18] WU Z P, JIAO L, WANG X L, et al. A self-powered deep-ultraviolet photodetector based on an epitaxial Ga_2O_3/Ga: ZnO heterojunction[J]. J Mater Chem C, 2017, 5(34): 8688–8693.

作者贡献声明：

王梓赫：提出研究方向、设计论文框架、绘制图表、参与数据分析与撰写论文；
张清风：完善论文框架，修订论文；
黄敏捷：实验测试、参与数据分析。

Preparation and Properties of Self-driven Ultraviolet Photodetectors Based on $Pb(Zr_xTi_{1-x})O_3$ Ferroelectric Materials

WANG Zihe, *HUANG Minjie*, *ZHANG Qingfeng*
(Hubei Key Laboratory of Micro-Nanoelectronic Materials and Devices, School of Materials Science and Engineering, Hubei University, Wuhan 430062, China)

Extended Abstract

Introduction With the advancement of the era, the demand for ultraviolet photodetectors in environmental monitoring and communication security continues to grow, leading to increasingly stringent performance requirements. In this case, self-driven ultraviolet photodetectors emerge to meet the needs of energy conservation and device miniaturization. However, conventional self-driven ultraviolet photodetectors still face some challenges such as low efficiency in photo-generated carrier separation, poor photoresponse performance, and limited response speed. Ferroelectric thin films with a high remnant polarization can form a depolarization field that penetrates the entire bulk material, enabling an effective separation of internally generated photo-generated electrons and holes. This provides a promising solution to the aforementioned issues. $Pb(Zr_xTi_{1-x})O_3$(PZT) is a typical ABO_3-type perovskite ferroelectric material. This material is widely used in ferroelectric memories, micro-electromechanical systems, and photodetectors due to its excellent ferroelectric, piezoelectric, and photoelectric properties. Extensive studies show that the composition significantly affects the crystal phase structure and ferroelectric properties of PZT thin films. However, its impact on the photoelectric performance requires a further systematic investigation. This work was to analyze the photoelectric characteristics of PZT thin films with different Zr/Ti ratios, in order to elucidate the influence of compositional modulation on the photoelectric effect.

Methods $Pb(Zr_xTi_{1-x})O_3$ ferroelectric thin films with different Zr/Ti ratios were prepared by a sol–gel method. The selected precursors and solvents were high-purity lead acetate [$Pb(CH_3COO)_2{\cdot}3H_2O$], zirconium n-propoxide ($C_{12}H_{28}O_4Zr$), and titanium isopropoxide ($C_{12}H_{28}O_4Ti$) as sources for lead, zirconium, and titanium, respectively, glacial acetic acid as a chelating agent, and n-propanol as a stabilizer. Semitransparent gold electrodes were deposited on the surface of the thin films by a model VZZ-300 high-vacuum thermal evaporation system (VANNO Co., China) to fabricate self-driven ultraviolet photodetectors with an Au/PZT/FTO vertical structure. The crystal structure of the films was characterized by a model D8 Advance X-ray diffractometer (XRD, Bruker Co., USA). The surface roughness of the films was determined by an atomic force microscope (AFM, Bruker Dimension Edge Co., USA). The optical properties of the films were analyzed by a model UV-3600 Plus ultraviolet-visible-near-infrared spectrophotometer (UV-Vis-NIR, Shimadzu, Japan). The ferroelectric properties were measured by a model Precision LC II ferroelectric test system (Radiant Co., USA). The current–time (*I*–*t*) curves were obtained by a model Keithley 2400 source meter, with a 150 W ultraviolet-enhanced xenon lamp as a light source.

Results and discussion The XRD patterns indicate that the three prepared PZT thin films with different Zr/Ti ratios all exhibit a typical perovskite structure, and no diffraction peaks from impurity phases appear aside from those originating from the FTO substrate. As the Zr content increases, the surface morphology of the films transitions from elongated needle-like structures to island-like structures, and finally to wavy undulations. The lowest root mean square (RMS) roughness of 2.62 nm is obtained at a Zr/Ti ratio of 0.52:0.48. The remnant polarization first increases from 27.9 μC/cm^2 (Zr/Ti=0.49/0.51) to a maximum of 33.2 μC/cm^2 (Zr/Ti=0.52/0.48), and then decreases to 31.1 μC/cm^2 (Zr/Ti=0.55/0.45) as the Zr content increases. A higher remnant polarization is beneficial to forming a stronger built-in electric field, thereby improving the separation efficiency of photogenerated carriers. The PZT films with different Zr/Ti ratios are all wide-bandgap semiconductors (>3.6 eV). As the Zr content increases, the bandgap widens from 3.60 eV to 3.68 eV, showing a blue-shift trend. When a negative poling voltage is applied, the depolarization field inside the PZT aligns with the built-in field induced by the interfacial Schottky barrier, synergistically enhancing the driving force for carrier

separation and leading to a significant increase in photocurrent. For the sample with a Zr/Ti ratio of 0.52:0.48 at a poling voltage of –2 V, the responsivity and detectivity reach 3.2 mA/W and 0.33×10^{11} Jones, respectively. Even under a weak illumination of as low as 0.17929 mW/cm^2, the device still generates a photocurrent of 1.02 nA, demonstrating the excellent detection sensitivity.

Conclusions $Pb(Zr_xTi_{1-x})O_3$ ferroelectric thin films with different zirconium-to-titanium ratios (*i.e.*, Zr/Ti=0.49:0.51, 0.52:0.48, 0.55:0.45) were fabricated by a sol–gel method, and self-driven ultraviolet photodetectors with an Au/PZT/FTO structure were constructed. The structural characterization revealed that all PZT thin films exhibited a pure perovskite phase with a good crystalline quality. The AFM analysis indicated that the film surfaces were smooth, dense, and displayed a uniform grain distribution. The ferroelectric property measurements further confirmed that all films with different Zr/Ti ratios showed characteristic ferroelectric hysteresis loops and possessed a high remnant polarization, having a maximum value of 33.2 μC/cm^2 at Zr/Ti=0.52:0.48. The results of photoelectric tests demonstrated that the device based on this optimal composition exhibited stable and reproducible photocurrent responses. At a poling voltage of –2 V, its responsivity and detectivity were significantly enhanced. In summary, the rational adjustment of the Zr/Ti ratio could effectively optimize both the ferroelectric properties of PZT thin films and the photoelectric characteristics of the corresponding devices. This work could innovatively utilize the inherent bulk depolarization field of PZT ferroelectrics as a driving force to achieve an efficient separation of photogenerated electron-hole pairs. Moreover, it could provide a systematic optimization strategy from the perspectives of compositional design and polarization modulation, offering an effective material- and physics-based solution to overcome the key bottlenecks of low responsivity and detectivity in self-driven ultraviolet photodetectors.

Keywords lead zirconate titanate; ferroelectric films; sol–gel; self-driven ultraviolet photodetectors